View metadata, citation and similar papers at core.ac.uk
brought to you by CORE
provided by NASA Technical Reports Server

COMBUSTION OF SOLID FUEL SLABS WITH GASEOUS OXYGEN IN A HYBRID MOTOR ANALOG

Martin J. Chiaverini, George C. Harting, Yeu-Cherng Lu, Kenneth K. Kuo
Nadir Serin, and David K. Johnson
Department of Mechanical Engineering, The Pennsylvania State University
University Park, PA 16802

ABSTRACT

Using a high-pressure, two-dimensional hybrid motor, an experimental investigation was conducted on fundamental processes involved in hybrid rocket combustion. HTPB (Hydroxyl-terminated Polybutadiene) fuel cross-linked with diisocyanate was burned with GOX under various operating conditions. Large-amplitude pressure oscillations were encountered in earlier test runs. After identifying the source of instability and decoupling the GOX feed-line system and combustion chamber, the pressure oscillations were drastically reduced from ±20% of the localized mean pressure to an acceptable range of ±1.5%. Embedded fine-wire thermocouples indicated that the surface temperature of the burning fuel was around 1000 K depending upon axial locations and operating conditions. Also, except near the leading-edge region, the subsurface thermal wave profiles in the upstream locations are thicker than those in the downstream locations since the solid-fuel regression rate, in general, increases with distance along the fuel slab. The recovered solid fuel slabs in the laminar portion of the boundary layer exhibited smooth surfaces, indicating the existence of a liquid melt layer on the burning fuel surface in the upstream region. After the transition section, which displayed distinct transverse striations, the surface roughness pattern became quite random and very pronounced in the downstream turbulent boundary-layer region. Both real-time X-ray radiography and ultrasonic pulse-echo techniques were used to determine the instantaneous web thicknesses and instantaneous solid-fuel regression rates over certain portions of the fuel slabs. Globally averaged and axially dependent but time-averaged regression rates were also obtained and presented. Several tests were conducted using, simultaneously, one translucent fuel slab and one fuel slab processed with carbon black powder. The addition of carbon black did not affect the measured regression rates or surface temperatures in comparison to the translucent fuel slabs.

INTRODUCTION

Hybrid rocket systems offer several advantages over their liquid and solid rocket counterparts that make them attractive alternatives for commercial and military applications. First, hybrid rockets require only half as much feed-system hardware as liquid propellant rockets, and therefore display improved reliability. Second, since they are much less sensitive to cracks and imperfections in solid fuel grains, hybrid rockets have safety advantages over solid propellant rockets. Third, hybrid rockets can be throttled for thrust control, maneuvering, and motor shutdown and restart. In addition, solid fuels are safer than solid propellants for manufacture, transportation, and storage. From a performance standpoint, hybrid rockets, in general, have specific impulse greater than solid rockets and density impulse greater than liquid bi-propellant rockets[1].

The key parameter in the study of hybrid rocket propulsion is the solid fuel regression rate and its dependence on various operating conditions. Many different regression rate models have been developed in order to explain the dependence of regression rate on operating conditions and flow parameters. In the early 1960's, Marxman and Gilbert[2] developed a regression rate model under the assumption that hybrid combustion is controlled by heat transfer from the flame zone to the solid fuel surface. Applying a two-zone boundary-layer model and utilizing a flame sheet to bridge the two zones, they found that the diffusion flame should be situated between 10-20% of the boundary-layer thickness above the fuel surface. Their regression rate equation was able to predict the axial dependence of a Plexiglas/GOX system when compared to experimental data which showed a minimum regression rate at a certain axial position in a circular port combustor. This minimum was attributed to the axial variations of total mass flux and Reynolds number based upon axial length. The review article by Muzzy[3] also presents a heat-transfer dominated regression behavior. Smoot and Price[4] studied the behavior of several polymer fuels in a laboratory-scale slab burner using combined fluorine and oxygen as an oxidizer. At low mass fluxes (G~10 Kg/m^2-s), the regression rates were found to be independent of pressure but dependent on G to the 0.8 power. The 0.8 power dependency was explained by turbulent flow relationships in circular ducts. At high mass fluxes (G~120 Kg/m^2-s) and/or low pressures, the regression rates were found to be nearly independent of mass flux but strongly

Approved for public release; distribution unlimited.

dependent on pressure. They attributed this pressure dependence to the rate–limiting chemical kinetic processes. Experimental data indicates that the regression rate may exhibit a dependence on pressure at either very high or very low mass fluxes. In the very low mass–flux regime, radiative heat transfer may account for the pressure dependence; however, at the very high mass–flux regime, reaction kinetics may become the rate–limiting mechanism. Some researchers[5] believed that the gas–phase reactions represent the rate–limiting step, while others[6] attributed the rate–limiting step to heterogeneous reactions at the fuel surface.

The presence of so many different types of models and correlations gives strong justification for obtaining more detailed experimental data for model validation. A more fundamental understanding of the complex processes involved in hybrid combustion is definitely needed in order to resolve the differences among various approaches and to develop a comprehensive theory. Furthermore, development of more reliable and accurate regression–rate correlations with applicability to broad ranges of operating conditions is needed for assisting the design of large–scale hybrid motors. Despite numerous investigations, very limited information exists concerning several pertinent phenomena, such as detailed reaction mechanisms between the gaseous oxidizers and decomposed fuel species, effect of ambient chemical species on solid–fuel pyrolysis processes, burning solid–fuel surface characteristics as functions of flow conditions, dependency of subsurface thermal wave profile on thermal properties of solid fuels, and influence of chamber operating conditions on instantaneous solid–fuel regression rates.

In an attempt to achieve fundamental understanding of some of these important issues, an experimental study on the fuel decomposition and boundary–layer combustion processes in hybrid rocket motors has been conducted at PSU. A high–pressure slab motor was designed and manufactured for conducting experimental investigations. Oxidizer (GOX) is injected through the head–end of the test chamber. In this paper, all reported data originates from experiments conducted using Hydroxyl–terminated Polybutadiene (HTPB) fuel consisting of R–45M supplied by Elf Atochem North America, and a cross–linking agent, Isonate 143L, supplied by Dow Chemical. In addition, several tests were conducted with fuel slabs processed with carbon black (0.25% weight) having a mean particle size of 75 nm. The carbon black acts as an opacifier to prevent in–depth radiation absorption. Fuel slabs were processed at PSU with fine–wire thermocouples embedded at various locations before curing. The study focuses on the following objectives: non–intrusive measurement of instantaneous and average solid fuel regression rate under various operating conditions including GOX flux level, motor pressure, and fuel formulation, determination of the solid–fuel surface temperatures and subsurface temperature profiles as a function of both operating conditions and axial location, and characterization of surface structure of the recovered solid fuel samples. The influence of carbon black powder as an opecifying agent on solid fuel regression rate and surface temperature was also examined. The problem of severe pressure oscillations in the motor was encountered early in the study and is addressed in this article.

EXPERIMENTAL FACILITY

Figure 1 shows a schematic diagram of the overall hybrid test rig, including a 2–D slab motor, a GOX supply system, and an ignition system. A computer code was developed to assist the design of the test motor. The code utilized a time–dependent continuity equation coupled with a chemical equilibrium code (CET–86) to determine fuel regression rate, oxidizer–to–fuel mass ratio, chamber pressure, and gas temperature. In order to meet the proper range of test conditions, parametric studies were conducted to determine the effect of oxidizer flow rate, nozzle diameter, test time, and fuel composition on motor operating characteristics. Based upon the results of the parametric study, a windowed 2–D hybrid motor was designed. The main body of the motor was constructed of stainless steel and weighed approximately 315.5 kg (700 lbs). It was designed to operate at up to 1300 psi. Gaseous oxygen can be injected at realistic flux levels of about 1.0 lb/in^2–s. The motor has an overall length of 1,067 mm, width of 178 mm, and height of 254 mm. The motor can be operated with either two opposing fuel slabs or one fuel slab with an opposing inert slab. The fuel slabs are 584 mm (23 in) long and 76 mm (3 in) wide. HTPB slabs processed at PSU can have a maximum usable web thickness of 20.5 mm (0.81 in), allowing an initial gap of 6.4 mm (0.25 in) between the slabs. For all tests conducted in this study, an initial gap of 12.7 mm (0.5 in) was used. The operating chamber pressure of the motor was partially controlled using interchangeable graphite exit nozzles.

The gaseous oxygen supply system consisted of a main feed line and a nitrogen purge line. Remotely operated ball valves were used to initiate and terminate the flow of oxygen, while a critical flow venturi was used to maintain a steady mass flow of GOX through the main line. The GOX flow rate was determined using the measured data from an upstream thermocouple and two pressure transducers located on either side of the venturi. For a given test, the flow rate was preset by adjusting the throat area of the venturi and the regulator setting of GOX supply line.

Filters in the GOX and nitrogen supply lines were employed to prevent any contamination of the system.

The ignition system consisted of a pair of high-pressure gaseous oxygen/methane pre-mixed torches and a pair of solid-propellant sticks to produce pilot flames in the upstream region of the solid fuel slabs. Flashback arrestors were used to prevent the occurrence of flame flashback in the pre-mixed sections of the igniter lines. The solid-propellant sticks were ignited electrically using nichrome wires connected to an AC transformer. Remotely operated solenoid valves were used to control the flow of oxygen and methane. Check valves and vents were installed in order to prevent the contamination of the gas bottles and any over pressurization of the system. Gaseous nitrogen was used to purge the ignition system after each test. After the initial system check-out tests, it was determined that successful ignition could be achieved using only the pilot flames generated by the solid-propellant sticks without activating the CH_4/O_2 torches. Thereafter, the ignition gas-supply lines were used primarily as an auxiliary nitrogen purge system, which was activated at the end of each test.

The motor (part of which is shown in Figure 2) has two sets of opposing windows. Each window is 280 mm (11 in) long by 44.5 mm (1.75 in) wide for real time X-ray radiography of the solid fuel regression phenomena. The motor was instrumented with a variety of diagnostic devices for determination of chamber pressure variations, subsurface thermal profile at various axial locations, burning fuel surface temperature distribution, and instantaneous web thickness of solid fuel slabs. Figure 2 shows the approximate locations of four of the seven thermocouples (TC), the pressure transducers (P) and the ultrasonic transducer (UST) in the instrumented motor. Other diagnostic tools, not included in this paper, can be utilized for measurement of gas velocity, flame temperature, and species concentrations at desired axial locations along the motor.

Static motor pressures were measured using 205 and 206 Setra pressure transducers, while several high-frequency Kistler 601B1 transducers measured dynamic motor pressures. An array of 25 μm fine-wire thermocouples (Pt/Pt-10%Rh) was embedded in the top fuel slab in order to measure solid-fuel subsurface temperature profiles and surface temperatures. The thermocouples were placed at pre-determined depths at several axial locations along the centerline of the fuel slab. The globally averaged solid-fuel regression rate was determined by weighing the fuel slabs before and after each test. In addition, the time-averaged, axially-dependent regression rate was deduced by measuring the pre- and post-firing fuel slab web thickness with a caliper at many axial stations.

The instantaneous solid fuel regression rate was obtained using two independent techniques: ultrasonic pulse-echo analysis and real-time X-ray radiography. Figure 3 is a block diagram showing major components of the ultrasonic pulse-echo system. A 1 Mhz-3/4" Panametrics Videoscan ultrasonic transducer (V114-RM) was placed behind the fuel slab within a fuel sample holder. The axial position of the transducer was selected from one of four locations. The transducer emits and receives ultrasound signals, and was connected directly to the Electronic Device for Ultrasonic Measurement (EDUM), supplied by ONERA, France. An oscilloscope was connected to the EDUM to provide a real-time visual record of the ultrasonic transducer signal, which was recorded on a video camera during each test run. At the same time, the ultrasonic signal was recorded by the data acquisition unit (Nicolet Multipro Transient Analyzer). Through a pre-test calibration procedure, the ultrasonic voltage signal was converted to the propagation time of the ultrasound pulse. The propagation time represents the time required for the pulse to travel from the transducer, through the fuel slab to the burning solid-fuel surface, and back to the transducer. As the fuel regressed, the propagation time of the ultrasound pulse decreased continuously due to the reduction of fuel web thickness. References 7 and 8 present in detail the operating principles of the ultrasonic pulse-echo method.

Figure 4 shows the schematic diagram of the real-time X-ray radiography system. During the test, an X-ray tube head emitted high-energy photons which passed through the LEXAN/MXB-360 window assemblies of the motor and then impinged on an image intensifier. Inside the motor, a portion of the X-ray photon energy was absorbed by the solid fuel when X-ray photons passed through the fuel slab region; however, the photons which passed through the port area experience little absorption. Because of this difference in the attenuation of the X-ray photons, the X-ray images displayed contrasting bright and dark regions, which showed the port area and fuel slabs, respectively. The instantaneous fuel web thickness was then deduced from these images. The principles of X-ray diagnostics of condensed phase combustion processes are given in Ref. 9.

DISCUSSION OF RESULTS

Table 1 below summarizes the test conditions of eleven test firings conducted in this study.

Table 1. Summary of eleven test firings.

Test No.	Fuel	$G_{ox,0}$, kg/m^2-s (lb/in^2–s)	Pressure, Mpa (psia)	Burn Time (s)	r_{global}, mm/s (in/s)
1	HTPB	337.8 (0.48)	8.55-2.31 (1240–335)	15.0	-
2	HTPB	68.3 (0.10)	2.07-2.05 (300–300)	2.7	-
3	HTPB	125.3 (0.18)	3.45-2.48 (500–360)	3.6	-
4	HTPB	166.8 (0.24)	8.96-1.79 (1300–260)	5.8	-
5	HTPB	158.3 (0.23)	5.31-2.82 (770–410)	4.1	1.4 (0.055)
6	HTPB	147.8 (0.21)	3.89-1.34 (565–195)	6.4	0.92 (0.036)
7	HTPB	105.6 (0.15)	3.65-1.72 (530–250)	9.0	0.76 (0.030)
8	HTPB	105.6 (0.15)	3.45-1.72 (500-250)	9.4	0.76 (0.030)
9	HTPB +0.25% cb	211.1 (0.30)	3.45-1.72 (500-250)	4.2	1.2 (0.047)
11	HTPB +0.25% cb	154.8 (0.23)	4.93-1.24 (715-180)	8.5	0.95 (0.037)

The pressure ranges given in the fourth column correspond to the maximum quasi–steady motor pressure (achieved at ignition) to the minimum motor pressure before shut down by terminating the GOX flow. The pressure drop of most test runs was due mainly to erosion of the graphite nozzle throat. Test No. 4 has an unexpected maximum pressure level of 8.96 MPa caused by a momentary blockage of the nozzle by a piece of solid fuel torn from the fuel slab. After this test, extension pins were mounted to the ends of the fuel sample holders to provide extra support for the solid fuel slabs. The third column of Table 1 gives the initial GOX mass flux found by dividing the known GOX mass flow by the initial combustor port area. The initial combustor port area was about 9.68 cm^2 (1.5 in^2) for all these tests. The last column gives the global regression rate of each test, obtained from pre– and post–test fuel slab weight measurements. Test No. 5 has a relatively high regression rate due to the large pressure oscillations observed during this test firing. Test Nos. 9 and 11 were each conducted using one translucent fuel slab and one fuel slab with 0.25% wt carbon black. No data is given for Test No. 10 because a different fuel formulation, not discussed here, was used for this test firing.

SUPPRESSION OF COMBUSTION INSTABILITY

Figure 5 shows a pressure–time trace of the hybrid motor during Test No. 2. The initial jump in pressure at about 0.2 seconds was caused by the start of GOX flowing through the supply line and into the hybrid motor. At a time of approximately 1.5 sec., the onset of ignition was achieved and flame began to spread over the solid fuel. Within about 0.5 seconds the chamber filling process was finished. At about 2.0 seconds after the start of the test, the motor reached a quasi–steady state operating condition of about 2.07 MPa (300 psia). During this period significant pressure oscillations, on the order to ±20% of the mean pressure, occurred. At about 4.3 sec., the GOX flow was shut off and the nitrogen purge was activated. The total time of combustion for this run was about 2.5 seconds. Figure 6 shows the frequency spectrum of the pressure oscillations. The combustion instability was observed in longitudinal modes. The fundamental (first) mode of oscillation occurred at a frequency of about 53 Hz, with a second mode at 106 Hz.

Similar to Test No. 2, significant pressure oscillations were observed in Test No. 1, 3, and 4. The major source of combustion instability was not fully determined at the end of these tests; however, it was speculated that the acoustic coupling between the GOX feed–line and combustion chamber could be responsible for the observed phenomena. Considering the distance between the choked venturi throat and the injector face of the combustion chamber, the calculated acoustic frequency in this equivalent 1/4–wave tube was around 50 Hz—very close to the fundamental mode frequency of 53 Hz. This close agreement seemed to indicate that the source of instability was associated with acoustic characteristics of the GOX supply line. Therefore, the following major modifications to the GOX supply line were made in order to eliminate the undesirable combustion instability phenomena:

1. A section of steel tubing in the GOX supply line between the venturi and the motor inlet was replaced. The new section was shaped in the form of a loop with a diameter of 40.6 cm (16 in). The effective length of the GOX

supply line was increased to verify the dependence of the oscillation frequencies on GOX supply line tube length. It was seen in Test No. 5 that the frequencies of the first and second longitudinal modes of oscillation were reduced to 40 and 86 Hz by the increase of GOX supply line length. The amplitude of oscillations for this run was also reduced to less than ±10%. This finding verified that the pressure oscillations in the motor were closely linked to the GOX supply line.

2. To further decouple the pressure wave transmissions between the motor and GOX supply line, and to damp out major pressure oscillations, a 6.35 cm (2.5") long orifice with inner diameter of 0.94 cm was added to the GOX supply line just upstream of the motor inlet. Since the GOX supply line had an inner diameter of 1.57 cm, the long orifice provided an area blockage ratio of about 65%.

Results from Test No. 6 and 7 showed that these two modifications successfully eliminated the combustion instability problems encountered in earlier tests of the hybrid motor system. Figure 7 shows the p–t trace of Test No. 6, which was conducted after both the loop and long orifice were installed. The pressure oscillations dropped to only about ±1% and ±1.5% of the mean pressure during Test No. 6 and 7, respectively. The chamber pressure showed significant decay after the attainment of the peak pressure in Fig. 7. This decay was caused by erosion of the graphite nozzle throat.

THERMAL PROFILES AND SURFACE CHARACTERISTICS OF BURNING SOLID FUELS

Figure 8 shows a temperature–time trace obtained using a 25 μm fine-wire Pt/Pt–10%Rh thermocouple embedded at 292 mm (11.5 in) from the leading edge of the upper fuel slab in Test No. 5. The thermocouple registered the ambient temperature for the first 0.6 second of the test run then began to register higher temperatures as the fuel surface regressed toward the thermocouple junction. The temperature profile increased smoothly until a temperature of around 1000 K was reached. Beyond the burning surface, the temperature profile undertook a rough, jagged shape in the gas–phase region, where the thermocouple bead location can be affected by cross flow of partially burned gases. The thermocouple was destroyed when it reached a temperature of around 1700 K at approximately 1.35 s. According to Ref. 10, the maximum temperature sustainable by the S–type thermocouples is around 1750 K.

Figures 9a and 9b show a pair of temperature–time traces recorded at two different axial locations (x = 14.0 and 44.5 cm measured from the front edge of the sample) during Test No. 6. In Fig. 9a, the upstream thermocouple displayed several temperature plateaus between 4.25 and 4.5 seconds. The first plateau corresponds to a temperature of about 900 K, which is believed to be the temperature of the melt layer covering the regressing solid fuel surface. This temperature plateau is associated with the passage of the thermocouple junction through the surface melt layer beneath the boundary layer. The local Reynolds number based upon axial distance is around 5.1×10^5, indicating the beginning of transition to turbulent boundary layer.

Comparing the temperature–time trace in Fig 9b with the upstream one (shown in Fig. 9a), it is apparent that the surface heat feedback from the gas phase is much stronger for the turbulent boundary–layer zone due to the increased mass flux in the axial direction and transverse motion of turbulent eddies. Thus, the surface temperature is higher, about 950 K, and the thermal profile in the subsurface region is steeper. The thermal wave thickness deduced for the upstream thermocouple was approximately 400 μm, while that at the downstream is about 250 μm. Corresponding to the higher energy feedback, the surface regression rate toward the rear end of the fuel slab was higher than that of the front section.

Similarly, Figs. 10a and 10b compare two fine–wire thermocouple traces recorded at upstream (x = 6.4 cm) and downstream (x = 52 cm) locations of the top fuel slab from Test No. 7. Again, the temperature profile recorded by the upstream thermocouple (definitely located in a laminar boundary layer covered station) shows a much thicker thermal wave (about 400 μm) than that of the downstream thermocouple (about 200 μm). The surface temperature in the upstream location, about 950 K, is lower than that of the downstream location, around 1000 K. In correspondence, the fuel slab at the upstream location has a lower regression rate than that of the downstream.

The recovered fuel surfaces also exhibit the transition from laminar to turbulent boundary layer with very distinct roughness patterns shown in Figs. 11a through 11c. In the upstream region, the solid fuel has a very smooth surface due to melt layer coverage. In the transition region surface striations (ripples) running in the transverse direction are clearly visible. In the downstream turbulent region, the surface roughness is greater in magnitude with a highly random pattern. Due to the high rates of heat feedback, the melt layer may or may not

exist in the turbulent boundary–layer region. The solid fuel could readily pyrolyze into gas–phase products without going through a liquefaction process.

SOLID FUEL REGRESSION RATE MEASUREMENTS

Figure 12 shows the axial variation of the time–averaged regression rates obtained from Test Nos. 5, 7, 8, 9, and 11. These results were obtained by measuring the fuel web thickness at many axial locations before and after these tests. Each set of data on the graph shows a relatively high regression rate near the front edge of the fuel slab and a minimum regression rate near the 13 to 15 cm location. After this minimum, the time–averaged regression rate increases along the fuel slab in the axial direction. This result is consistent with the fact that the total mass flux increases with distance along the slab. Following the increase in mass flux, the rate of heat feedback to the burning solid–fuel surface increases in the axial direction, resulting in higher regression rate. The front edge of the fuel slab has a relatively high regression rate because the flame zone in the boundary layer is close to the fuel surface in the very upstream region, where the boundary layer is quite thin. The initial decrease in regression rate leading to the minimum rate in the 13 to 15 cm region may be due to the competing effects of total mass flux, G, and Reynolds number based on axial distance, Re_x, as suggested in Ref 1. Theoretically, the regression rate of the fuel should increase with G, which increases with x, but decrease with $Re_x^{-0.2}$, which decreases with x. The minimum point of regression should correspond to the crossover of these two effects. The high regression rate at the trailing edge is believed to be caused by the recirculating flow before the entrance of the aft mixing chamber. It is interesting to note that Test No. 5 shows a jump in regression rate at the 230 mm (9 in) location. This jump is believed to be caused by a rapid increase in heat flux to the fuel surface due to the onset of the turbulent boundary layer.

Figure 13 shows the deduced instantaneous regression rate and measured instantaneous regressed web thickness obtained from the ultrasonic pulse–echo system for Test No. 7. The ultrasonic transducer was located at 254 mm (10 in) downstream of the front edge of the fuel slab. The regression rate was relatively high in the beginning of test, but decreased continuously with time after attaining its peak value. The time variation of the instantaneous regression rate at a particular axial location is quite consistent with the time variation of the mass flux, which is relatively high in the beginning of the test since the combustor port area is relatively small. The instantaneous web thickness regressed as recorded by the EDUM increased smoothly and monotonically during the test. The slope variation of the instantaneous web burned also indicates a faster regression rate in the beginning of the test. For this test, the ultrasonic pulse–echo method gives a total regressed web thickness of about 5.8 mm at the transducer location, while direct measurements at the same location using a caliper gave a value of 6 mm. These values represents a difference of 3.4%.

The real–time X–ray radiography system was also utilized to determine the instantaneous regressed web thickness. Figure 14 compares the X–ray and ultrasound results obtained from Test No. 7. The X–ray results correspond to a location 12.7 cm (5 in.) downstream from the front edge of the fuel slab. The ultrasonic transducer was located 25.4 mm (10 in.) downstream of the front edge of the fuel slab. Although these measurement were made at different locations, the distance between them is not too large. As shown in Fig, 14, these results agree fairly well. The instantaneous regressed web thickness obtained from X–ray data shows the same trend as that of the corresponding ultrasonic data, but exhibited a slightly lower value. This difference is expected due to the upstream location of the X–ray data station. The total web thickness regressed at this location was found to be 5.8 mm from the X–ray system, while measuring the fuel slab thickness before and after the test with a caliper gave a value of 5.6 mm. The difference in these measurements is 3.5%.

Figure 15 shows the instantaneous regressed web thickness at a location 12.5 cm from the front edge of the fuel slab obtained from X–ray radiography data of Test No. 11. In order to obtain the corresponding instantaneous regression rate at this location, the data is fit with an equation of the form

$$w = a + bt^m + ct^n \tag{1}$$

where w is the instantaneous regressed web thickness, t is time, and a, b, c, m, and n represent the constants to be determined. The double power–law form of Eq. (1) fits the data very well, as shown in Fig. 15. Taking the time derivative of Eq. (1) yields the regression rate:

$$r = bmt^{m-1} + cnt^{n-1} \tag{2}$$

This procedure can be performed at many individual stations along the fuel slabs. Figure 16 shows the instantaneous regression rate results at several axial locations for Test No. 11. Each regression rate starts relatively high at the beginning of the test, decreases rapidly, then decreases more slowly as the test continues.

EFFECT OF CARBON BLACK ADDITIVE

In order to determine the effect of in–depth radiation absorption on fuel regression rate and solid fuel surface temperature, one of the fuel slabs was fabricated with the addition of carbon black powder (0.25% by weight) during the fuel processing stage in order to make the HTPB fuel sample opaque for both Test No. 9 and 11. The carbon black powder was obtained from Cabot Industries and had a mean particle size of 75 nm. Carbon black acted as an opacifier to prevent any in–depth radiation absorption in the fuel slab during combustion. Any radiative heat transferred from either the hot combustion gases or from soot particles to the fuel slab should then be absorbed at the fuel slab surface.

The global fuel regression rate was found by weighing each fuel slab before and after the tests. The results of both tests indicated no significant difference in the regression rates of the translucent and black fuel slabs. For Test No. 9, with an initial GOX flux of 0.30 lb_m/in^2–s, both slabs had an overall regression rate of 1.2 mm/s. In addition, both slabs displayed very similar time–averaged regression rate profiles with respect to axial location. For Test No. 11, which had an initial GOX flux of 0.23 lb_m/in^2–s, both slabs had nearly the same regression rate of 0.96 mm/s. Again, the time–averaged regression rate profiles with respect to axial location were found to be quite similar. Taken together, the results of these test firings suggest that in–depth radiation absorption was not a significant contributor to the regression rate of the HTPB fuels slabs. One possible explanation for this observations is that a black char layer was formed immediately on the surface of the translucent fuel slab shortly after ignition, so that the radiative heat flux was absorbed only at the surface rather than in the interior of the slab.

Several Pt/Pt–10%Rh 25 μm fine–wire thermocouples were used to obtain the fuel slab subsurface temperature profile and surface temperature of the fuel slab processed with carbon black for Test No. 11. One of the thermocouples indicated that the surface temperature was about 930 K at a location 30 cm downstream from the front edge of the fuel slab. This result is consistent with previous surface temperature measurements, which indicate that the surface temperature of the HTPB fuel slabs is around 900 to 1050 K, depending on operating conditions and axial location. The subsurface thermal wave profiles of Test No. 6 (translucent slab) and 11 (black slab) may be compared since both tests had similar GOX mass fluxes (0.21 and 0.23 lb_m/in^2–s, respectively) and global regression rates (0.92 and 0.95 mm/s, respectively). As shown in Figure 17, the surface temperature and subsurface temperature profile is quite similar to the corresponding case from Test 6 (shown in Figs. 9a and 9b), giving further evidence that the addition of carbon black powder did not affect the performance of the HTPB fuel slabs.

SUMMARY AND CONCLUSIONS

A high–pressure, 2–D slab motor was designed and tested for conducting fundamental studies on hybrid combustion of solid fuels. The test motor was instrumented with various diagnostic devices. An oxidizer/fuel combination of GOX/HTPB was used in all tests. Major findings are listed below.

- Severe combustion instability phenomena were encountered in early tests. The source of instability was identified as the acoustic coupling between the GOX feed line and the combustion chamber. The instability problem was eliminated by decoupling the two regions. The magnitude of chamber pressure oscillations was reduced to less than ±1.5%.

- The burning surface temperature of the HTPB varied between 900–1050 K, depending on both operating conditions and axial locations.

- The subsurface temperature profiles are steeper (thinner thermal waves) with higher surface temperatures at the downstream locations; this is due to the increase in heat transfer rates in the turbulent portion of the boundary layer.

- Regression rate increases with axial distance, except near the leading edge portion of the solid fuel; this is caused by the increase in total mass flux and convective heat flux.

- Both ultrasound and x-ray results indicate that the regression rate varies substantially with both time and axial location; generally decreasing with time and increasing with axial location from the leading edge.

- The addition of carbon black to HTPB fuels did not affect the fuel regression rate, surface temperature, and subsurface thermal wave profile in comparison to the translucent fuel slabs. This implies that the in-depth radiation absorption was not important to the regression rate. Radiation flux was absorbed only at the surface where a black char layer is formed.

- The recovered fuel samples showed distinct surface structures at different axial regions. The surface covered by a laminar boundary layer is very smooth, indicating the existence of a liquid layer. The transition region showed transverse striations and the turbulent boundary-layer zone exhibited very rough surface structure with highly random patterns.

ACKNOWLEDGMENTS

The authors would like to thank NASA/MSFC for funding this work under Contract No. NAS 8-39945. The support and encouragement of Mr. Roger Harwell of MSFC and Mr. Marion D. Kitchens of NASA Headquarters are highly appreciated. We would like to thank Mr. Les Tepe of the Phillips Lab and Dr. David M. Mann of the Army Research Office for supporting the purchase of the Ultrasonic Measurement System from ONERA, France. Under the NATO/AGARD sponsorship, the help of Mr. Franck Cauty of ONERA in the technology transfer of the ultrasonic pulse-echo technique to the research team is also greatly appreciated. The authors also wish to thank TUBITAK of Turkey for sponsoring the scholarship of Mr. Nadir Serin which made his participation in this study possible. The efforts of Jon Foremsky are highly appreciated.

REFERENCES

1. Sutton, G. *Rocket Propulsion Elements: An introduction to the Engineering of Rockets*, Sixth Edition, John Wiley & Sons, New York, 1992.

2. Marxman, G. A. and Gilbert, M., "Turbulent Boundary Layer Combustion in the Hybrid Rocket", Ninth International Symposium on Combustion, p. 371, Academic Press, Inc., New York, 1963.

3. Muzzy, R. J., "Applied Hybrid Combustion Theory", AIAA paper 72–1143, 1972.

4. Smoot, L. D., and Price, C. F., "Regression Rates of Nonmetallized Hybrid Fuel Systems", AIAA Journal, Vol. 3, No. 8, 1965.

5. Wooldridge, C. E., Marxman, G. A., and Kier, R. J., "Investigation of Combustion Instability in Hybrid Rockets", Final Report NASA CR–66812, Contract NAS 1–7310, 1969.

6. Ramohalli, K. and Stickler, D. B., "Polymer–Degradation Theory of Pressure Sensitive Hybrid Combustion", Thirteenth Symposium (International) on Combustion, pp. 1059–1077, The Combustion Institute, 1970.

7. Cauty, F., et. al., "Determination of Solid Propellant Burning Rate Sensitivity to the Initial Temperature by the Ultrasonic Method", *Non–Intrusive Combustion Diagnostics*, Edited by K. K. Kuo and T. P. Parr, Begell House, Inc., New York, 1994.

8. Dijkstra, F., Korting, P., and van der Berg, R., "Ultrasonic Regression Rate Measurement in Solid Fuel Ramjets", AIAA Paper 90–1963, 1990.

9. Kuo, K. K. and Parr, T. P., eds., *Non–Intrusive Combustion Diagnostics*, Begell House, Inc., New York, 1994, pp. 365–423.

10. Anon, *The Temperature Handbook*, Omega Engineering, Inc., 1995.

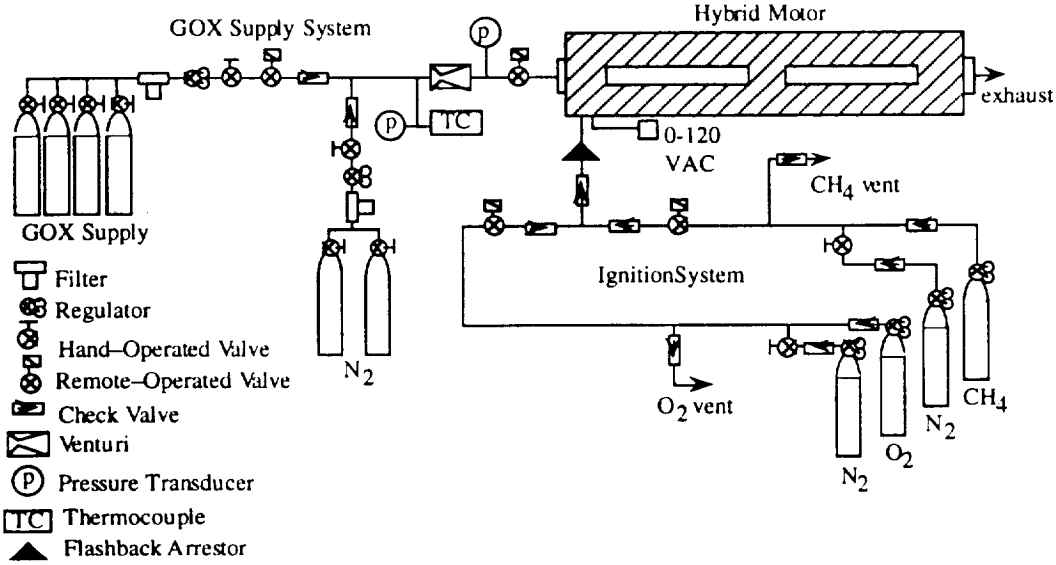

Figure 1. Schematic Diagram of Hybrid Motor Test Facility.

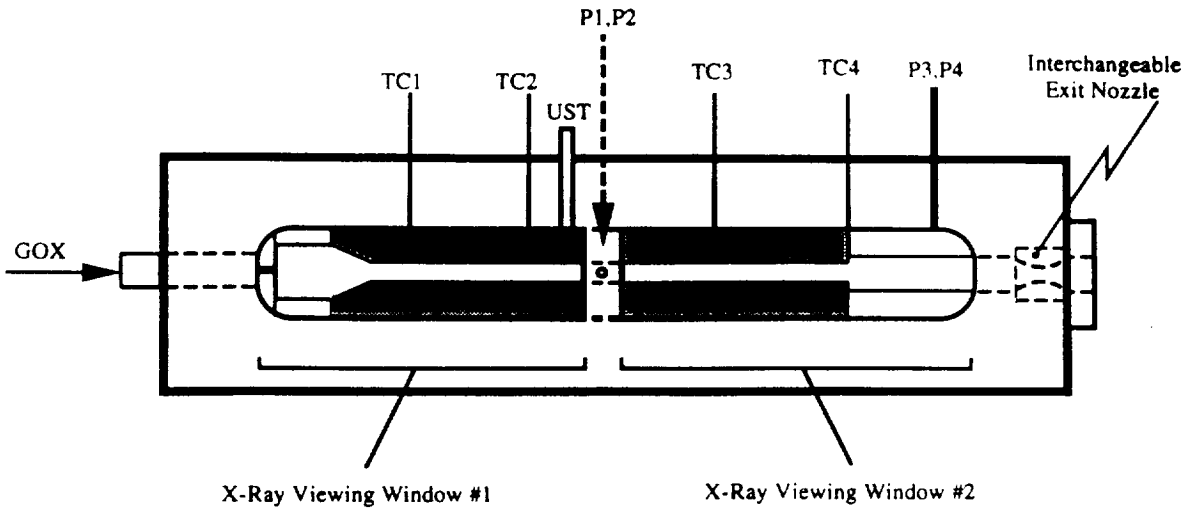

Figure 2. Instrumentation Of A Two Dimensional Windowed Hybrid Motor.

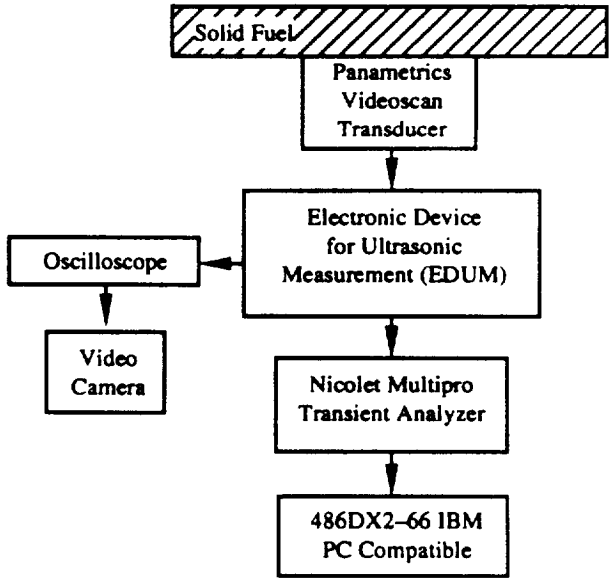

Figure 3. Block Diagram for Ultrasonic Pulse-Echo System.

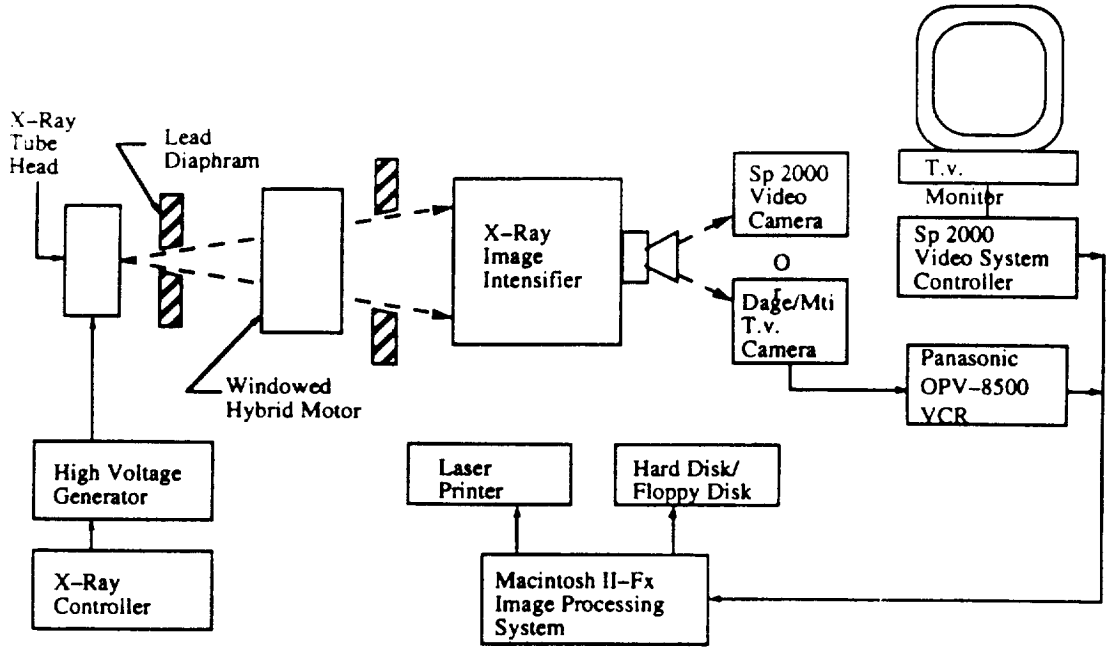

Figure 4. Block Diagram for Real-time X-ray radiography System.

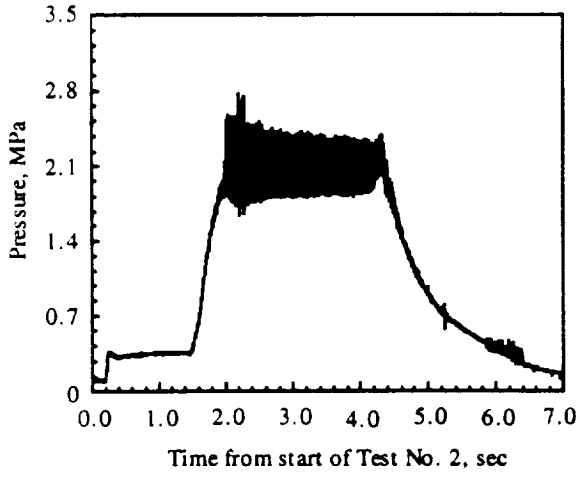

Figure 5. Motor pressure-time trace from Test No. 2.

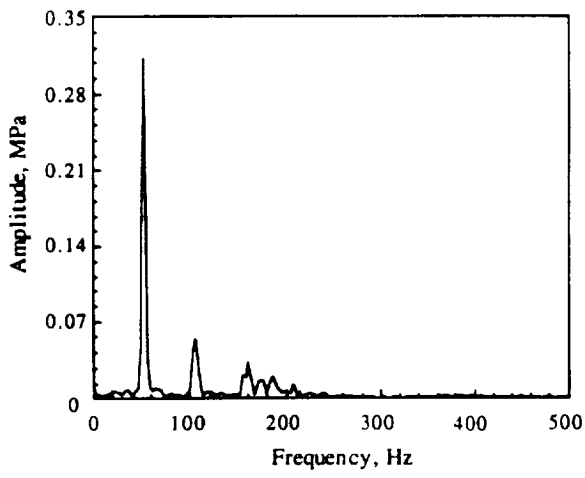

Figure 6. Frequency spectrum analysis of pressure-time trace of Test No. 2.

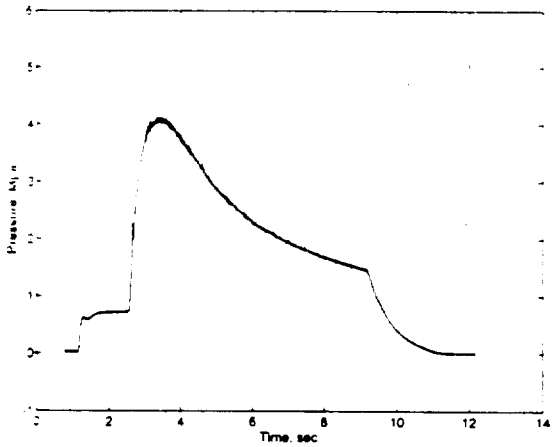

Figure 7. Motor pressu · time trace from Test No. 6.

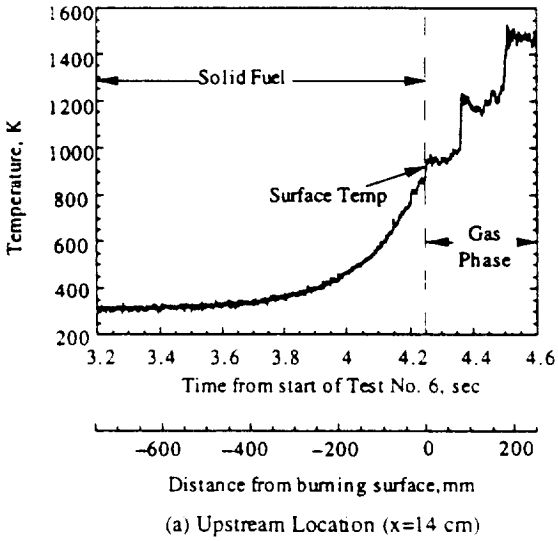

(a) Upstream Location (x=14 cm)

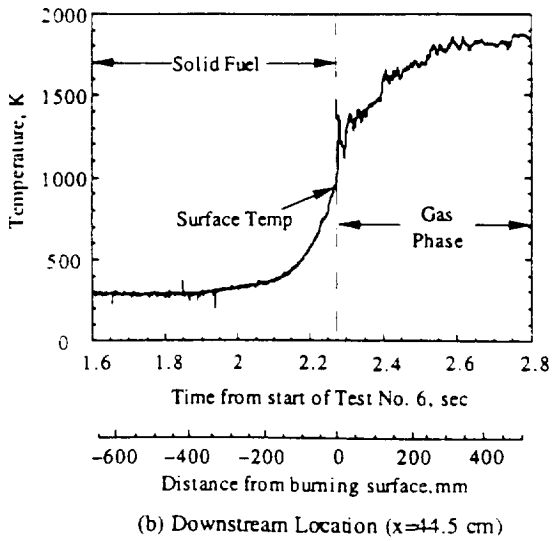

(b) Downstream Location (x=44.5 cm)

Figure 9. Temperature profiles at two axial locations from Test No. 6.

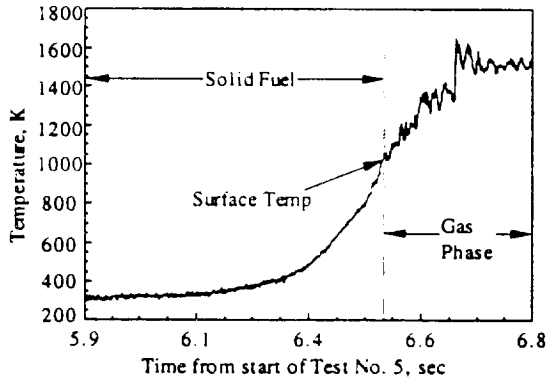

Figure 8. Temperature–time trace for Test No. 5.

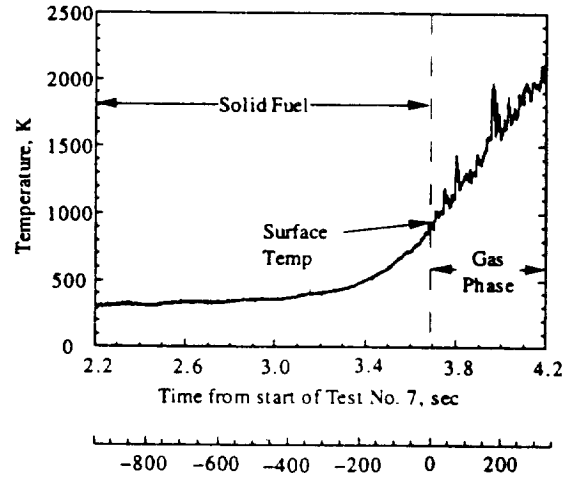

(a) Upstream Location (x=6.4 cm)

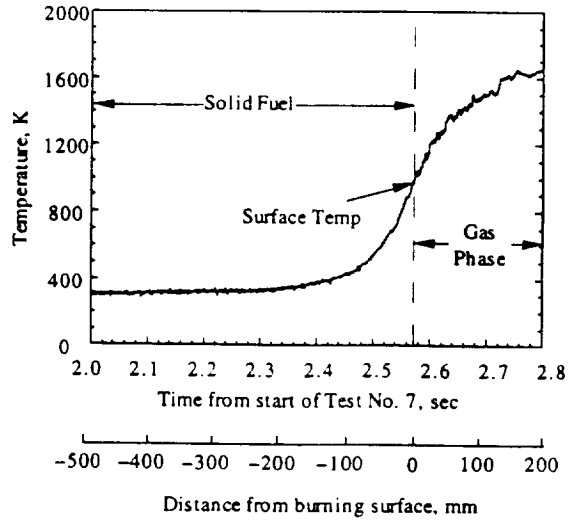

(b) Downstream Location (x=52 cm)

Figure 10. Temperature profiles at two axial locations from Test No. 7.

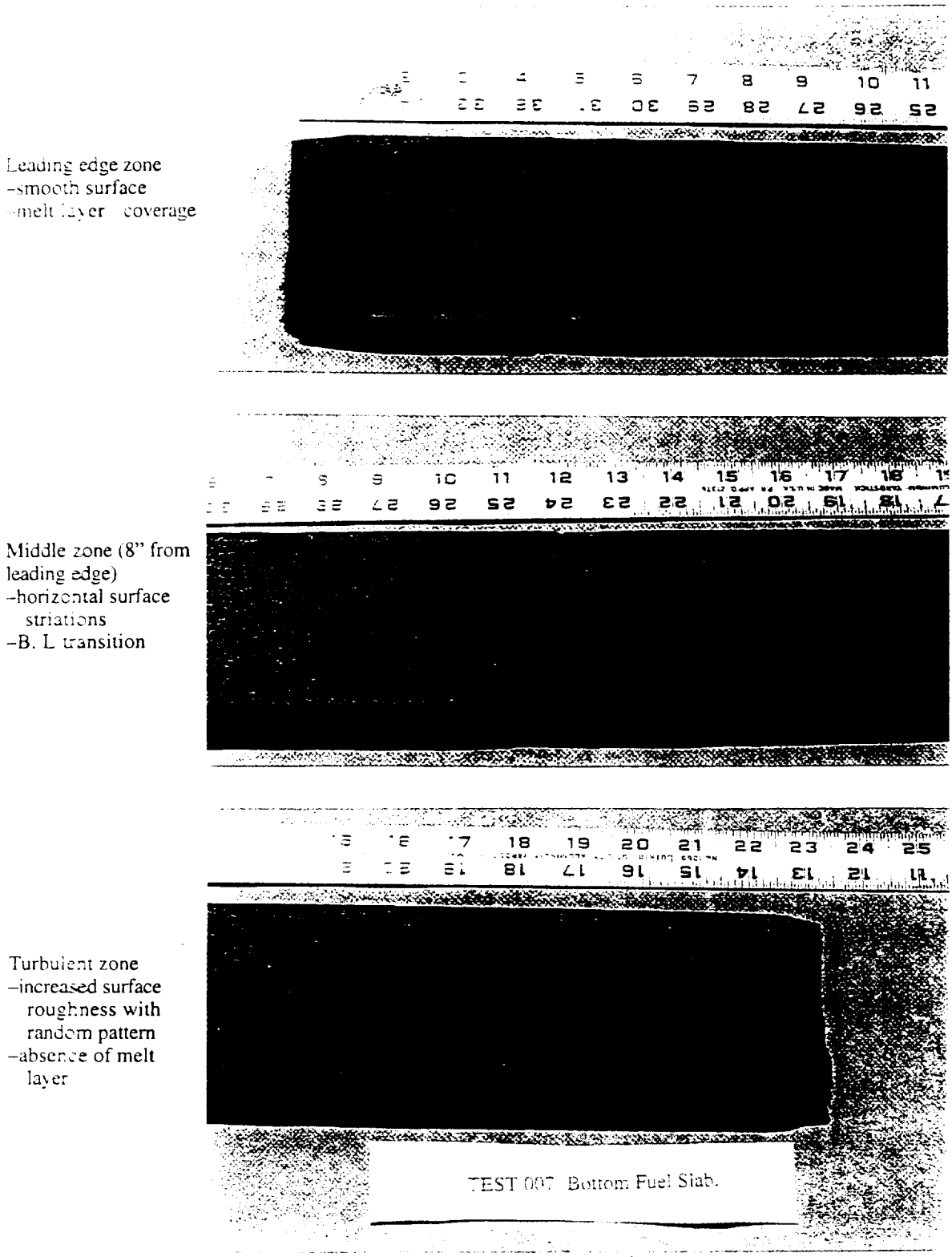

Figure 11. Recovered fuel sample surface for Test No. 7.

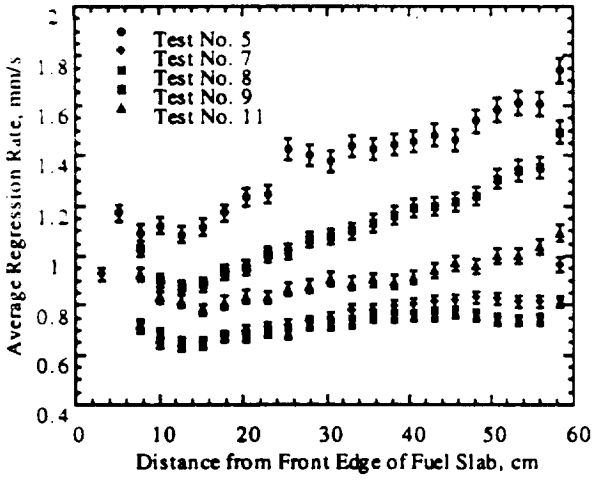

Figure 12. Regression rate profiles for Test Nos. 5, 7, 8 9, and 11.

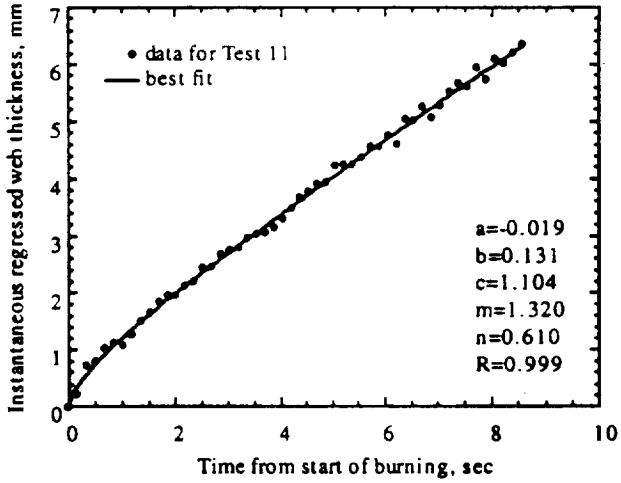

Figure 15. Burned web thickness and curvefit at x=12.5 cm for Test 11.

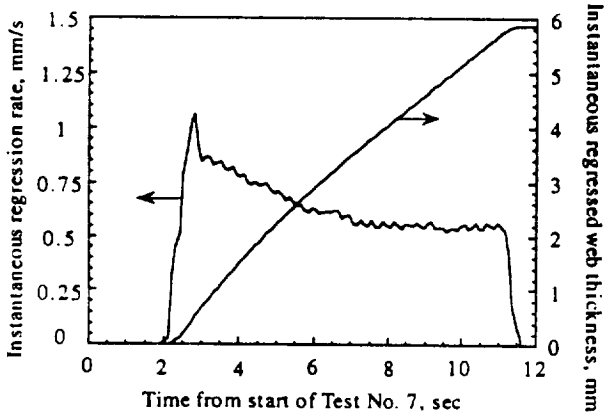

Figure 13. Instantaneous regression rate and burned web thickness for Test No. 7.

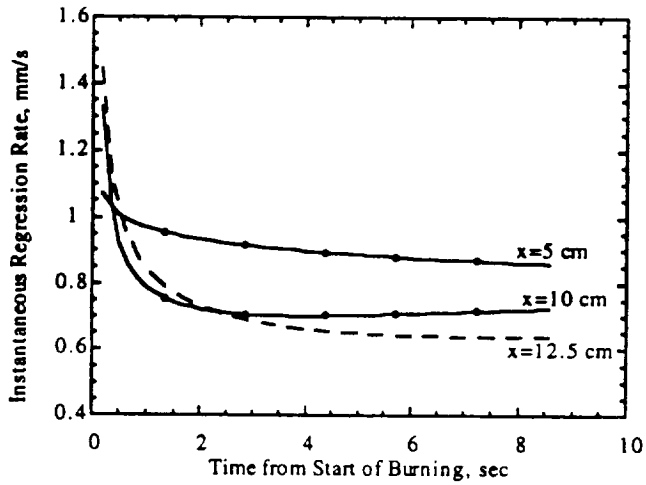

Figure 16. Instantaneous regression rates at several axial locations for Test No. 11.

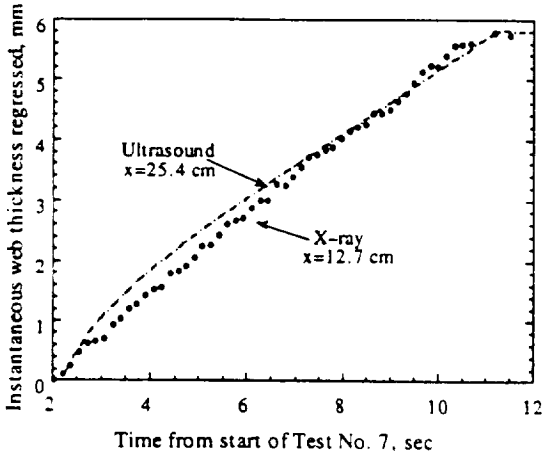

Figure 14. Comparison of X-ray and ultrasound results of instantaneous web thickness burned for Test No. 7.

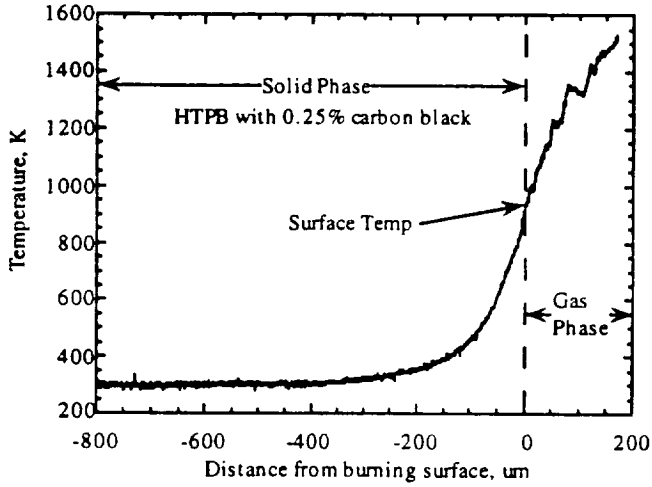

Figure 17. Temperature–time trace for Test No. 11 at x=30 cm.